

Anticorrosive Multi-band 5G Wireless Communication and THz Electromagnetic-Interference Shielding with Graphene Assembled Film

Rongguo Song

Hubei Engineering Research Center of RF-Microwave Technology and Application

Boyang Mao

University of Cambridge

Zhe Wang

Wuhan University of Technology

Ning Zhang

Hubei Engineering Research Center of RF-Microwave Technology and Application

Ran Fang

Hubei Engineering Research Center of RF-Microwave Technology and Application

Jingwei Zhang

Hubei Engineering Research Center of RF-Microwave Technology and Application

Yuen Wu

University of Science and Technology of China <https://orcid.org/0000-0001-9524-2843>

Qi Ge

Chongqing 2D Materials Institute <https://orcid.org/0000-0002-1493-6120>

Kostya Novoselov

University of Manchester

Daping He (✉ hedaping@whut.edu.cn)

Hubei Engineering Research Center of RF-Microwave Technology and Application, Wuhan University of Technology <https://orcid.org/0000-0002-0284-4990>

Article

Keywords: graphene assembled film, 5G technology, flexible electronics, wireless communication, electromagnetic protection

Posted Date: November 11th, 2021

DOI: <https://doi.org/10.21203/rs.3.rs-965162/v1>

License:  This work is licensed under a Creative Commons Attribution 4.0 International License.

[Read Full License](#)

Abstract

Since first developed, the conducting materials in wireless communication and electromagnetic interference (EMI) shielding devices have been primarily made of metal-based structures. Here, we present a highly conductive and corrosion-resistant graphene assembled film (GAF) that can be used to fabricate multi-band 5G wireless communication electronics and EMI protection at frequencies ranging from tens of MHz to THz to demonstrate its potential in metal replacement in practical electronics. The GAF based antennas (dipole antenna, ultra-wideband antenna and 5G wireless communication antenna array) are comparable with metal-based antennas in terms of performance and device complexity. The EMI shielding effectiveness of GAF can reach up to 127 dB in the frequency range of 2.6 GHz - 0.32 THz, and a maximum shielding effectiveness per unit thickness is of 6966 dB/mm. Furthermore, the GAF metamaterials exhibit promising frequency selection characteristics and angular stability as flexible frequency selective surfaces that can work at 3.5 GHz and 60 GHz respectively.

Introduction

The matured development of 5G and emerging 6G wireless communication electronics (WCE) has the potential to revolutionise many applications such as healthcare¹, fitness monitoring², wearable communication^{3,4}, Internet of Things⁵, e-skins^{6,7}, and so on, making our lives more convenient, safe and productive. To efficiently transport electrical signals and electromagnetic waves at multi communication bands, the 5G and 6G networks require more antennas, much larger bandwidths, and a higher density of base stations than previous generations of communication networks. As a result, the demand for WCE will skyrocket in the approaching years: for example, the number of global 5G base stations is expected to reach 65 million by 2025⁸. Together with the explosive growth of WCE devices, particularly mobile terminals, serious issues of electromagnetic interference (EMI) have also arisen, which can lead to signal loss, data misinterpretation, and even system failure⁹. The increased electromagnetic pollution can also be hazardous to human health¹⁰.

In general, the electrical conducting component in WCE devices and effective EMI shielding materials require high electrical conductivity as well as high electron mobility¹¹. Metals have such characteristics (with electrical conductivity of over 10^7 S/m and electron mobility of 10 - 50 $\text{cm}^2/\text{V}\cdot\text{s}$)¹², so previous WCE devices and EMI shielding materials have conventionally been made from metal-based structures for decades^{13,14}. However, with the growing demands for being flexible and highly integratable, anticorrosive, lightweight, smaller in size, easy-to-fabricate, and operating at higher frequency communication bands (from dozens of GHz to THz), the metal material based structures are beginning to show less ability to cope with next generation WCE and EMI shielding requirements¹⁵. In addition, due to the pollutants and CO₂ emission generated during metal mining and manufacturing processes¹⁶, sustainable development in the next generation consumer electronics becoming essential due to the growing environmental impacts associated with the electronic waste (e-waste)¹⁷.

Metal free WCE devices and EMI shielding material are, however, challenging to make since it is hard to have a material simultaneously matching the high electrical conductivity and presenting good mechanical stability. In recent years, carbon based electronics, especially the possibility of exploiting graphene to assemble macroscopic structures has been demonstrated as a feasible approach to reach the target^{18,19}. Previous research demonstrated that graphene can be directly grown, implanted or printed on a substrate to form a composite structure^{20,21}. However, the conducting graphene layer in these structures typically has limited thickness or low conductivity, which results in high surface resistance and poor device performance^{22,23}. Recent breakthroughs in the reduction of graphene oxide²⁴ and exfoliation of pristine graphene²⁵ have demonstrated that graphene assembled structures can reach electrical conductivities of up to 10^5 S/m²⁶⁻²⁸, and that such techniques can be applied in WCE^{29,30}. Such electrical conductivity, however, is still two orders of magnitude lower than that of metal-based materials. Meanwhile, MXene, as a unique family of two-dimensional transition metal carbides and/or nitrides, can be used as an alternative materials to achieve this goal. MXene has a high electrical conductivity (around 10^5 S/m) and can provide effective electromagnetic shielding performance with low thicknesses^{9,31} as well as be applied in WCE³². However, MXene are easily oxidised (unsuitable for long-term use) and difficult to produce in large quantities³³, which limits its application in real-world commercial products. Furthermore, so far, both graphene and MXene-based WCE devices and EMI shielding materials have only been demonstrated as concept validations with simple functions, no practical and advanced electronics have been designed or systematically compared with metal-based commercial devices in terms of robustness and device performance, etc. yet^{34,35}.

Here, we report a scalable production of graphene assembled film (GAF) with a conductivity of 2.58×10^6 S/m, and applied it in next generation WCE and EMI shielding materials. After 100,000 bending tests (with a bending radius of 1.5 mm), GAF film can retain its high flexibility and conductivity, with no structural damages. To investigate GAF's capabilities in 5G technology and flexible electronics, we first demonstrated its stable performance in 5G WCE as flexible coplanar waveguide transmission lines and 1/4 wavelength resonators under various twisting conditions. GAF-based dipole antennas have a -39 dB reflection coefficient and a high gain of 1.89 dBi, which is comparable to copper-based antennas. Furthermore, GAF antenna is highly anticorrosive: after two weeks of salt spray treatment, it retains its $|S_{11}|$ and gain, whereas metal-based antennas lose over 4.68 dBi for their gain. We also investigate an integrated wearable 5G communication system based on all-GAF flexible electronics, including a flexible wearable antenna, filter and a 2x2 antenna array. An ultra-wideband antenna (with bandwidth ratio 25:1) and a 5G antenna array with 140 antenna elements (with high gain of 24.23 dBi and promising sidelobes below -20 dB) are also designed and built for millimetre wave electronics. For EMI shielding performance, GAF is investigated over a frequency range of 2.6 GHz - 0.32 THz. GAF has an electromagnetic shielding effectiveness (EMI SE) of up to 127 dB in the low frequency band (2.6 GHz - 40 GHz) and more than 80 dB in the high frequency band (40 GHz - 0.32 THz), and with a maximum EMI SE per unit thickness of 6966 dB/mm. Furthermore, two flexible frequency selective surface (FSS) based on GAF are designed, operating at 3.5 GHz and 60 GHz, respectively, and exhibiting good frequency selection characteristics

and angular stability. Thus, our research demonstrates GAF's full potential as a sustainable alternative material in multi-band 5G communication electronics and EMI shielding for next-generation wireless communication electronics.

Results

2.1. GAF Fabrication and Characterisation

To achieve graphene-based laminates with a high electrical conductivity, we introduce extremely large flake size graphene oxides (LGO) as the film's building precursor to reduce the contribution of contact resistance. Fig. 1a is a schematic diagram of the fabrication process. The detailed fabrication procedures are described in **Methods**. With commercially standard equipment, GAF can be manufactured in a viable and scale manner, Supplementary Fig. 1-2³⁶. Fig. 1b is a transmission electron microscope (TEM) image presents a typical LGO sheet with a lateral size of 108 μm . In the corresponding size distributions curve from optical microscope measurement, Fig. 1c, the average LGO lateral size is around 110 μm , which is significantly larger than any previously reported study^{37,38}. To compare, films made from typical size GO flakes, Supplementary Fig. 3, have also been fabricated as a control experiment and been tested accordingly. GAF was manufactured by an optimised compression and secondary high temperature (2850°C) graphitization process. The XRD (Fig. 1d) and Raman spectroscopy (Fig. 1d and Supplementary Fig. 4) confirm GAF's highly graphitized and defect free structure. Based on Raman measurement, a large crystallite size $L_a = 1967.95$ nm in the GAF is also confirmed according to Equation 1³⁹.

$$L_a(\text{nm}) = (2.4 \times 10^{-10}) \lambda_l^4 \left(\frac{I_D}{I_G}\right)^{-1} \quad (1)$$

Small-angle x-ray scattering (SAXS) patterns of GAF, inserted in Fig. 1e, show a prismatic scattering pattern indicating GAF with highly aligned layered structure. In contrast, for typical flake size GO assembled film (TGF), Supplementary Fig. 5, no such pattern is identified⁴⁰. Supplementary Fig.6 is the top view GAF SEM image, microfolds are uniformly distributed on the GAF surface. As shown in Supplementary Fig. 7, the cross-section SEM images of the GAF characterise a thin film with thickness of $\sim 19 \pm 0.5$ μm . This thickness is similar to commercial copper foil applied in consumer electronic devices .

The electrical conductivity of all samples is measured by a four-probe method (Supplementary Fig. 8 and Supplementary Video 1). In Supplementary Fig. 9, the electrical conductivity of GAF and TGF fabricated under different conditions are characterized. The conductivity of GAF is $2.58 \pm 0.06 \times 10^6$ S/m, which is 5 times higher than that of graphite film (5×10^5 S/m) and about 2 times higher than HOPG (1×10^6 S/m) and TGF (9×10^5 S/m), as shown in Fig. 1e. In Supplementary Fig.10, the electron transfer pathway between GAF and TGF is proposed as the mechanism for this ultrahigh electrical conductivity⁴¹. 5G WCE are powered by radio frequency (RF) signal, for which skin depth effect cannot be negligible. To better

integrate in 5G WCE electronics, the thickness of conducting material in the device always demands a thickness of around 20 μm or below. The skin depth δ can be calculated by the following Equation 2.

$$\delta = \frac{1}{\sqrt{\pi f \mu \sigma}} \quad (2)$$

where f is the frequency, μ is the permeability and σ is the conductivity of conductive material. For non-magnetic conducting materials, μ is taken as $4\pi \times 10^{-7}$ N/A². Taking the Radio Frequency Identification (RFID) communication frequency band (860 MHz) specified in EPC Gen2 standard as an example, to reduce the resistance loss, the thickness of conductive material should be greater than skin depth. Regarding this, in Fig. 1f, a selective area which requires materials having electrical conductivity higher than 0.75×10^6 S/m is identified. For non-metal materials, it can be found that among all novel developed materials, only graphene films made by high temperature (over 2500 °C) annealing can meet these requirements (Supplementary Fig. 11 and Supplementary Table 1-2.). Although metal materials, like gold (Au), silver (Ag), copper (Cu), aluminium (Al) and iron (Fe), has higher electrical conductivity, the apparent density of GAF (1.92 g/cm³) is significantly lower, shown in Supplementary Fig. 12-13. In Fig. 1g and Supplementary Video 2, we demonstrate that GAF can retain its ultrahigh conductivity even after 100,000 bending cycles test with a bending radius of 1.5 mm. The SEM images show the durability of GAF that can endure a zigzag folding without any breakage (Supplementary Fig. 14-15). A similar test was performed on a commercial copper foil with the thickness of 20 μm ; the copper foil broke after only 12 folds (Supplementary Fig. 16).

To verify the excellent flexibility of GAF electronics, a flexible coplanar waveguide transmission line (FCPW TL) and a $\lambda/4$ short-circuited resonator based on silica gel film (Supplementary Fig. 17) are first designed and fabricated. As shown in Fig. 1h-i, FCPW TL's transmission characteristics of the being bent and twisted at different conditions are investigated between the 10 MHz - 12 GHz frequency band., It is found that bending and twisting has negligible effects on the transmission coefficient ($|S_{21}|$) of GAF transmission line. Fig. 1j-k illustrate the $|S_{11}|$ (between 10 MHz to 12 GHz band) of GAF $\lambda/4$ short-circuit resonator in the original state and different twist states. Like GAF flexible transmission line, the twist does not change the resonator's performance.

2.2. GAF as a Dipole Antenna and its Highly Anticorrosion Properties

A GAF dipole antenna is used in this study as an example to compare with metal antennas in terms of device performance and corrosion resistance, which is a continuing concern in next-generation WCE working at higher frequencies and operating powers. Fig. 2a is the digital photo of GAF dipole antenna and copper antenna in the same pattern (design details in **Methods** and Supplementary Fig. 18). The measured gain of antennas in the 0.7 GHz - 1.0 GHz frequency band and at 865 MHz are shown in Fig. 2b-c, respectively. The GAF antenna has a gain of 1.89 dBi, which is comparable to the copper antenna of 1.94 dBi. This gain is much higher than that of graphite antenna (1.05 dBi), HOPG antenna (1.39 dBi), and TGF antenna (1.35 dBi). Fig. 2d-e present the 3D and 2D radiation patterns of GAF antenna at 865

MHz, also indicating a matching performance with copper antenna. The measurement environments for the antennas are exhibited in Fig. 2f-g. In Fig. 2h, the GAF dipole antenna exhibits the highest gain of any graphene-based dipole antenna reported in the literature⁴²⁻⁴⁶. In supplementary Fig. 19, the E-field distribution simulation results of the graphene dipole antenna in different phases indicates the current on the dipole arm is sinusoidally distributed.

The salt spray treatment is applied to the GAF and copper antennas to investigate their corrosion resistance, Supplementary Fig. 20. Fig. 2i-j are the digital photos of GAF antenna and copper antenna after one week's and two weeks' salt spray: the copper antenna is rusted and then broken after the test, but the exterior of GAF antenna is unaffected. Fig. 2k illustrates the simulated and measured reflection coefficient $|S_{11}|$ at resonant frequencies of 865 MHz of the initial GAF antenna and after the salt spray treatments. The -10 dB bandwidth (BW) of the GAF antenna is from 790 MHz to 980 MHz, which covers the RFID communication frequency band. After salt spray treatment, the GAF's $|S_{11}|$ does not change. However, the $|S_{11}|$ of copper antenna becomes only -6.25 dB at 865 MHz after two weeks of salt spray, Fig. 2l-m presents the measured gain at 865 MHz of GAF and copper antennas during the test, the gain of the GAF antenna is unchanged, but the copper antenna has a significantly lower gain of -2.74 dBi after two weeks of salt spray. This test confirms that, unlike metal based materials, because graphene is naturally more anticorrosive, no additional anti-corrosion coating is required in the GAF WCE to protect it from corrosion, which simplifies manufacturing and reduces weight.

2.3. Wearable Communication System and 5G Millimeter Wave Antenna with GAF

Fig. 3a illustrates the division of wireless communication spectrum with specified applications. Sub-6 GHz is currently the most mainstream mobile communication frequency band, such as 2.45 GHz in the Industrial Scientific Medical (ISM) frequency band and 3.5 GHz in the 5G communication frequency band⁴⁷. In this work, we confirm that GAF antennas can be used to directly replace metal-based antennas in commercial sub-6 GHz electronic devices, like mobile phone and drone, without losing functionality, as shown in Fig. 3b-g, Supplementary Fig. 21-22, and Supplementary Video 3-4. To demonstrate GAF are capable of fabricating flexible Sub-6GHz WCE, we build an integrated terminal and base mobile communication system with all GAF based WCE, including flexible GAF wearable antenna, 2×2 GAF antenna array and GAF filter, as shown in Supplementary Fig. 23. The radiation patterns of GAF antenna and antenna array recorded for every 10° of rotation in microwave anechoic chamber, Fig. 3h. In Supplementary Fig. 24-25, a communication system integrated with all above GAF electronics is demonstrated. The gain and transmission coefficient of the flexible 5G GAF antenna and antenna array are measured, as shown in Fig. 3i. The gain of the two antennas reaches the maximum at the resonant frequency of 2.45 GHz, which is consistent with the measured $|S_{21}|$ (as in Fig. 3i, blue line). The measured results show that the GAF 5G WCE communication system can function reliably, and that the flexible 5G GAF antennas and transmission line are capable to fit and work on the human body to transmit signals.

Millimeter wave WCE, with the advantages of high directivity, small in size, high resolution, rich spectrum resources, and high information security, is an essential technology for the 5G mobile communication⁴⁸.

To investigate GAF's abilities in millimeter wave 5G WCE, GAF-based 5G ultra-wideband (UWB) antenna and 5G antenna array are studied. Fig. 3j-k illustrate the geometry and present a digital photograph of the proposed 5G UWB antenna. The measured -10 dB bandwidth covers the frequency range of 1.6 GHz to 40 GHz with the bandwidth ratio of 25:1, Fig. 3l. Although the test frequency is up to 40 GHz, the actual impedance bandwidth of the 5G UWB antenna is much wider. To gain insight into the radiation characteristics, we simulated the surface current distribution of the UWB antenna at 6 GHz, 10 GHz, 20 GHz, and 40 GHz. As shown in Supplementary Fig. 26, current distribution demonstrates that the UWB antenna is working in its fundamental resonance mode at low frequency band and in higher resonance mode at high frequency band. A GAF 5G millimeter wave antenna array with the geometrical dimensions of 135 mm × 95 mm × 0.54 mm is fabricated, shown in Fig. 3m-n and Supplementary Fig. 27. The GAF 5G antenna array has 140 antenna elements (14 × 10), which accords with the Chebyshev current distribution. Fig. 3o illustrates the simulated and measured $|S_{11}|$ and gain from 25 GHz to 27 GHz. The GAF 5G antenna array operates at 26 GHz with a $|S_{11}|$ of -22.54 dB. The measured highest gain is 24.23 dBi, which matches with the simulated results. Fig. 3p-q and Supplementary Fig. 28 depict the measured E-plane and H-plane radiation patterns. Due to the anisotropy of GAF, the antenna array has a sidelobe performance below -20 dB in E-plane and H-plane: the beam width and sidelobe level of the E-plane and H-plane, respectively, are 8.5°, -21.76 dB and 5.9°, -24.94 dB. The simulated 3D radiation patterns of the GAF 5G antenna array at 26 GHz are shown in Fig. 3r, which also confirms the excellent sidelobe performance.

2.4. GAF for EMI Shielding

The EMI shielding performance of GAF in the frequency range of microwave band, millimeter wave band and terahertz (THz) band is explored. Firstly, the EMI shielding effectiveness (SE) at the frequency range of 2.6 GHz - 40 GHz is simulated and tested by the rectangular waveguide method, Supplementary Fig. 29-30. Fig. 4a-c show the EMI SE of the GAF and commercial copper foils. The thickness of EMI SE produced from commercial copper foils (we tested thicknesses of 10 μm and 50 μm) has little effect on their EMI performance and presents an EMI SE of around 100 dB in the 2.6 GHz - 40 GHz frequency band. This is due to the fact that copper fully reflects electromagnetic waves and the absorption effect is negligible. Due to the high conductivity, GAF exhibits ultra-high EMI SE. Additionally, because of its natural laminate structure, which causes absorption and multiple internal reflections⁹, increasing the thickness of GAF can improve the EMI SE. The proposed GAF's EMI shielding mechanism is in Supplementary Fig. 31. GAF's EMI SE with a thickness of 15 μm is greater than 80 dB and can achieve 90-100 dB above 6 GHz. When the thickness increase to 50 μm, the EMI SE of GAF rises to around 110 - 120 dB, especially at 13.5 GHz, where it reaches up to 127.3 dB. When the frequency exceeds 26 GHz, the GAF with a thickness of 15 μm exhibits the same EMI SE as copper foil with a thickness of 50 μm. Furthermore, We use the free space method (Supplementary Fig. 32) to evaluate GAF's EMI shielding performance over the frequency ranges of 40 GHz-67 GHz, 75 GHz-110 GHz, and 0.22 THz-0.325 THz. As shown in Fig. 4d-f, GAF outperforms copper foil in terms of EMI shielding as frequency increases. The EMI SE of the GAF with a thickness of 15 μm and 50 μm is around 60 - 80 dB and 80 - 100 dB, respectively, which is higher than the

40 - 60 dB of copper foil. We compared the recently reported EMI shielding performance of graphene-based and other materials, as shown in Fig. 4g. GAF is the electromagnetic shielding material that is closest to the ideal area, with the highest SE in the same thickness and the thinnest thickness in the same SE. Due to the importance of thickness to EMI shielding materials, SMI SE per unit thickness (SE/t) is used to characterize the EMI performance. Among other graphene structures, carbon nanotubes, carbon fibres, and MXene, GAF has the highest SE/t (6966 dB/mm), as shown and compared in Fig. 4h and Supplementary Table 3.

2.5. GAF Applied in FSS at Sub-6 GHz and Millimeter Wave Frequencies

In addition to complete electromagnetic shielding, selective shielding of the electromagnetic field is also important in many cases to ensure the normal transmission of other frequency bands. As a member of metamaterials, frequency selective surface (FSS) is formed by periodic arrangement of structural units, which can selectively absorb, reflect and transmit electromagnetic waves⁴⁹, and thus is an effective way to realize frequency selection. To further explore the electromagnetic protection performance of GAF, we developed two transparent, flexible FSS that work in Sub-6 GHz and millimeter wave bands, respectively. Firstly, a miniaturized flexible FSS based on GAF that works at 3.5 GHz is designed, Supplementary Fig. 33. The GAF FSS is with 12×12 periodic elements, fabricating by a high precision laser engraving. The structure dimensions are 192 mm×192 mm×0.075 mm, as shown in Fig. 5a, with the optimised parameter values shown in Supplementary Fig. 34 and Table 4. GAF FSS is translucent and has a very low areal density of 0.0087 g/cm². GAF FSS is very flexible and can conform to curved surfaces. Because of the presence of the bending line, the edge of the periodic element structure has a strong parasitic capacitance, as shown in Supplementary Fig. 35, which can miniaturise the FSS. A high parasitic capacitance can also assist FSS maintain its angular stability. The equivalent circuit diagram of the GAF FSS element is shown in Supplementary Fig. 36. The transmission coefficient results of the periodic element are shown in Supplementary Fig. 37. The FSS has a resonance frequency of 3.5 GHz, agreeing with the simulation results. In Fig. 5b, the E-field distribution can be used to investigate the working mechanism of FSS. It is clear that the FSS resonates at 3.5 GHz and generates a large induced current, preventing electromagnetic waves from passing through the FSS. The measured transmission coefficient and shielding efficiency of GAF FSS under normal incidence of electromagnetic wave is shown in Supplementary Fig. 38-39. Supplementary Fig. 40 is the measuring environment. In the 3.38 - 3.91 GHz frequency band, the transmission coefficient of GAF FSS is less than -10 dB, which means that FSS can shield more than 90% of electromagnetic waves. In particular, GAF FSS can shield 99.4% of electromagnetic waves at 3.5 GHz. Outside of this frequency band, electromagnetic waves can pass GAF FSS in a large proportion, proving that GAF FSS has good frequency selection characteristics. Fig. 5c are the spectrum curve of GAF FSS at different incident angles of electromagnetic waves, the transmission coefficient and working bandwidth of GAF FSS remain essentially constant in the 0-25° range, indicating that GAF FSS has high angular stability.

We also designed a low profile and ultra-wideband flexible millimeter wave FSS with a thickness of 0.138λ. The element structure of millimeter wave FSS is illustrated in Supplementary Fig. 41. The digital

photos shown in Fig. 5d and Supplementary Fig. 42 demonstrate the FSS's flexibility. The FSS has the physical dimensions of 125 mm × 125 mm × 0.065 mm implanting with 1600 elements. Supplementary Fig. 43 illustrates the simulated transmission coefficient. GAF millimeter wave FSS covers a wide -10 dB bandwidth of 8.16 GHz between 55.76 GHz and 63.92 GHz. Supplementary Fig. 44 is the surface current distribution of the GAF millimeter wave FSS at 60 GHz. It can be seen that the FSS resonates at 60 GHz and generates a strong induced current, hindering the passage of electromagnetic waves at 60 GHz. Supplementary Fig. 45 shows the measured transmission coefficient and shielding efficiency of GAF millimeter wave FSS under normal incidence of electromagnetic wave. The GAF FSS can shield 99.9% of electromagnetic waves at 60 GHz. Different bending states of GAF FSS and incident angles of electromagnetic waves can be achieved by varying the distance between two brackets and rotating the disc. As shown in Fig. 5e, the frequency selection performance of GAF FSS remains stable within a bending angle changing between 0° to 40°. Fig. 5f illustrates that GAF FSS maintains good frequency selection performance in the range of electromagnetic waves ± 30° incident angle.

Discussion

Here, we demonstrate a lightweight, flexible, mechanically ultra-durable, highly chemically stable, and ultrahigh conductive GAF that can be applied in 5G multi-band wireless communication electronics and electromagnetic protection to overcome the major issues in metal-based electronics. These GAF-based 5G electronics can be designed into a variety of sophisticated patterns and integrated communication systems to achieve a wide range of advanced functions across the entire microwave communication frequency band. GAF has also demonstrated excellent electromagnetic shielding performance in the microwave and terahertz frequency bands, and it can be designed and fabricated into metamaterials to achieve selective electromagnetic wave shielding. Our research demonstrates that the highly conductive graphene film can be used as an alternative fully functional and sustainable material in radio frequency fields, which can support current and next-generation flexible electronics, WCE, and EMI shielding applications.

Methods

GAF fabrication. Two major approaches have been utilized to achieve high electrical conductivity of graphene-based laminates. Firstly, we maximized the size of graphene crystallites, which allowed us to reduce the contribution of contact resistance. Secondly, we introduced secondary annealing process and special assembly technique which allows highly laminated, defect free assembly of such graphene crystallites into continuous films. Firstly, graphene oxide (GO) was prepared *via* the modified Hummers method. The extremely large flake size graphene oxide (LGO) was separated and collected, and use as the film fabrication precursors. The LGO was separated from graphene oxide suspension (3 wt. %) after seven times repeating centrifugation (the bottom 30% GO are collected each time). An LGO lateral size statistical study is carried out by optical microscope: LGO with the lateral size > 75 μm accounts for 74%, and 54 % of the LGO are > 100 μm. The typical flake size graphene oxide (TGO) was used as it was

synthesised and applied as a control experiment. LGO assembled film was prepared through pre-metered roll transfer coating of LGO hydrogel on a self-released substrate such as polyethylene terephthalate (PET) films. Subsequently, the LGO hydrogel on substrate was heated (70-80°C) for drying. Thereafter, a soft, dark brown free-standing and paper-like graphene oxide film (LGO film) could be easily peeled off from the PET substrate. In this step, the anisotropic liquid crystalline behaviour of LGO hydrogel can lead to a pre-aligned orientation structure after force directed rolling transfer. This highly ordered laminate can be converted into a pristine graphene film in meters long scale *via* a high temperature graphitization process. LGO film was thermally annealed at 1300°C for 2 hours and 2850°C for 1 hour in Ar atmosphere between two graphite plates for reduction and graphitic crystallisation. The giant crystalline graphitic domain size in graphene assembled film (GAF) is formed by the coalescence of neighbouring reduced LGO sheets⁵⁰. Graphene films are fully graphitized after primary high temperature annealing, allowing dangling-bond-free graphene nanosheets to tile on each other with broad-area plane-to-plane contacts. A rolling compression with the pressure of 300 MPa was further introduced to obtain the final GAF. The following rolling compression contributes to eliminate inter layer gaps and contact resistance, also leads to an excellent flexibility. Followed by the rolling compression, a secondary high temperature annealing process at 2850°C in Ar atmosphere was carried out to further remove the structural damage during the rolling process to increase the electrical conductivity⁵¹. TGF was obtained with same method but from the TGO.

GAF WCE fabrication. Laser engraving (with high resolution up to micrometre scale) was proposed and investigated to manufacture sophisticate GAF patterns (Supplementary Fig. 45). First, the GAF and the dielectric substrate (FR-4, Silica gel film, Rogers 5880, PET) were combined by hot pressing to form GAF Printed Circuit Board (PCB)²⁹. To adapt the laser engraving machine, the carving patch of the device dimensions output by the simulation software was calculated using LPKF CircuitPro PL 2.0. The GAF devices were manufactured in one step by a laser engraving machine (LPKF Laser & Electronics ProtoLaser S) using the calculated laser path.

Dipole antenna design and measurement. The dipole antenna was designed on the FR-4 substrate having a thickness (h) of 1.6 mm and dielectric constant of 4.4. Both the width (W) of the arm and the gap (g) between the two arms were 3.53 mm, and the arm length (L) was 63.95 mm. For the convenience of testing, two arms of the dipole antenna were connected by a SMA connector *via* conductive adhesive. To verify the performance of the GAF antenna, antennas made by graphite, HOPG, TGF and copper with same design were carried out for comparison. The reflection coefficient was measured in a microwave anechoic chamber with a Network Analyzer (PNA, Keysight N5247A). The gain was calculated by placing two identical antennas in microwave anechoic chamber and measuring the forward transmission coefficient ($|S_{21}|$) according to the following formula

$$|S_{21}|_{dB} = P_L + 2G(dB)$$

$$P_L = 20 \log\left(\frac{\lambda}{4\pi r}\right)$$

4

Where P_L is path loss in dB, λ is the wavelength at the resonant frequency, G (dB) is the antenna gain with respect to an isotropic source, $r=2.8$ m is the distance between two antennas. The measurement frame diagram is shown in Supplementary Fig. 46. The radiation patterns were tested using the antenna measurement system (Diamond Engineering Automated Measurement Systems). The GAF antenna was placed on the rotating platform as a receiver, and the standard reference antenna (REF antenna) was fixed at the same level as a radiator. The data was recorded for every 10° of rotation. All measurements were performed in a microwave anechoic chamber.

Flexible coplanar wave guide transmission line, $\lambda/4$ short-circuit resonator design and measurement. The flexible coplanar wave guide transmission line (FCPW TL) and $\lambda/4$ short-circuit resonator were designed on the substrate of silica gel film has a thickness of 1.5 mm and loss tangent of 0.06, as depicted in Supplementary Fig. 12. The dielectric constant and loss tangent of silica gel were measured by the coaxial method (KEYSIGHT 85051-60007). The length and width of the FCPW TL and resonator were 100 mm and 11mm, respectively. The GAF strips were 3 mm in width and 1mm apart. The S-parameters were measured with a Network Analyzer (PNA, Keysight N5247A). The transmission coefficient is very low at high frequency, this is because the loss of the substrate is large, and the FCPW TL does not have a good impedance matching with the PNA measurement system.

Wearable antenna design and measurement. The substrate of the microstrip antenna was silica gel film with a thickness of 1.5 mm. The length and width of patch were 31.37 mm and 40.37 mm, respectively. In order to achieve miniaturization, the GAF antenna adopted a 50Ω microstrip embedded feeding structure, and the width of the feeding microstrip line was 3.32 mm. The patch and ground were made of flexible GAF.

Design and measurement of 2×2 antenna array. The 2×2 antenna array was designed on the FR-4 substrate. The length and width of element patch were 28.53 mm and 37.26 mm, respectively. In order to reduce mutual coupling and grating lobe, the distance between the two elements was 0.7λ , and the parallel feed network was used. T-type power divider and quarter wavelength impedance converter were selected to realize impedance matching of antenna array. The patch and feed network of the antenna array were GAF. The reflection coefficient was measured with Network Analyzer (PNA, Keysight N5247A). The radiation patterns were tested using the antenna measurement system (Diamond Engineering Automated Measurement Systems) in microwave anechoic chamber. The GAF antenna array was placed on the rotating platform as a receiver, and the standard reference antenna (REF antenna) was used as a radiator. The data is recorded for every 1° of rotation.

Design and measurement of filter. The substrate of GAF filter was FR-4 with thickness of 1.6 mm. The GAF filter was a fifth-order Chebyshev low-pass filter with a 3 dB cut-off frequency of 3.5 GHz. The filter

was a microstrip structure, and the input port and output port impedance were both 50 ohms. The microstrip line and ground were made of flexible GAF. The optimized dimensions were $L=34.1\text{mm}$, $l_1=6.5\text{mm}$, $l_2=1.75\text{mm}$, $l_3=2.46\text{mm}$, $l_4=3.2\text{mm}$, $W=24.6\text{mm}$, $w_1=15.72\text{mm}$, $w_2=3.06\text{mm}$, $w_3=0.24\text{mm}$. The S-parameters were measured with a Network Analyzer (PNA, Keysight N5247A).

Design and measurement of UWB antenna. The UWB antenna was designed on a RT5880 substrate with a relatively permittivity of 2.2, loss tangent of 0.0009 and a thickness of 0.254 mm. To reduce the size, a semi-circular monopole acts as a radiator. The UWB antenna was fed by a micro-strip line with the length of $F_L=20\text{mm}$ and width of $F_W=0.8\text{mm}$. The characteristic impedance of the micro-strip was 50 ohms. It is worth mentioning that designing a slot ($G_L \times G_W$, 0.7 mm \times 1 mm) in the ground plate can better achieve impedance matching and increase the working frequency range. The patch and ground were made of flexible GAF. The reflection coefficient was measured with a Network Analyzer (PNA, Keysight N5247A) in microwave anechoic chamber.

Design and measurement of millimeter wave antenna array. The substrate of millimeter wave antenna was Rogers 5880 with thickness of 0.508 mm. The length and width of element patch were 3.41 mm and 4.35 mm, respectively. The antenna array contains 14 \times 10 antenna elements and adopts Chebyshev current distribution to suppress the sidelobes of the antenna array. At the resonance frequency, each array element has the same radiation phase. The patch and ground were made of flexible GAF. The reflection coefficient was measured with Network Analyzer (PNA, Keysight N5247A). The radiation patterns were tested using the antenna measurement system (Diamond Engineering Automated Measurement Systems). The GAF millimeter wave antenna array was placed on the rotating platform as a receiver, and the standard reference antenna (REF antenna) was used as a radiator. The data was recorded for every 0.125° of rotation. All measurements were performed in microwave anechoic chamber.

Measurement of EMI SE. A series of rectangular waveguides are used to measure the electromagnetic interference shielding performance of GAF in WR-284, WR-187, WR-137, WR-90, WR-62, WR-42, WR-28 bands. The GAF is carved to a specific dimension as test sample to fit the rectangular waveguide. A foam with the same length and width and a thickness of 2 mm is used to support the GAF test sample. The vector network analyzer (Keysight PNA N5247A) is used to record the transmission coefficient and reflection coefficient of the rectangular waveguide test sample. According to the S-parameter, the EMI SE, reflectance and transmittance of the test sample can be calculated. Before the test, we qualitatively studied the EMI shielding performance of GAF through simulation. In the 40 GHz-0.32 THz frequency band, the free space method is used to test the EMI SE of GAF. The two ports of the vector network analyzer (Keysight PNA N5247A, N5256AW10, N5256AW03) are connected to the horn antenna to measure the EMI SE of GAF.

Design and measurement flexible frequency selective surface. The GAF with a typical thickness of 15 μm is selected as the conductor of Sub-6 GHz and millimeter wave FSS. PET film with a thickness of 0.06mm, dielectric constant of 3.5 and loss tangent of 0.003 is the substrate of GAF FSS. The performances of GAF FSS were measured in the microwave anechoic chamber to avoid the influence of

external electromagnetic wave. The two horn antennas were placed in opposite directions. The vector network analyzer (Keysight PNA N5247A) records the reflection coefficient and transmission coefficient of the two antennas to calculate the frequency response of the GAF FSS. Firstly, the transmission coefficient of the two horn antennas without FSS was measured. The GAF FSS was then placed between the two horn antennas, and the transmission coefficient was measured again. Subtracting two results was the corresponding transmission coefficient for GAF FSS. In order to reduce the electromagnetic wave reflection of the bracket, a certain area of absorbing material was wrapped around the horn antenna. The GAF Sub-6 GHz FSS and millimeter wave FSS were placed on a rotatable disc and fixed by two horizontally movable brackets and a rotatable wooden shelf respectively in order to test the performance of the FSS under different bending states and different incident angles of electromagnetic waves.

Declarations

Acknowledgements

This work was financed by the National Natural Science Foundation of China (Grant No.: 51672204, 51701146), the Fundamental Research Funds for the Central Universities (WUT: 2020-YB-032, 205209016 and 2020IB005).

Author contributions

R.S., B.M. and D.H. conceived and designed the research project. R.S., Z.W., N.Z. and R.F. carried out the experiments. J.Z., Y.W. and Q.G. helped analyze the data. R.S., B.M., K.N. and D.H. wrote the paper. All authors discussed and approved the manuscript.

Competing Interests

The authors declare that they have no known competing financial interests or personal relationships that could have appeared to influence the work reported in this paper.

Supplementary materials

Supplementary data associated with this article can be found in the online version.

References

1. Kim, J., Campbell, A. S., de Ávila, B. E. & Wang, J. Wearable biosensors for healthcare monitoring. *Nat. Biotechnol.* **37**, 389–406 (2019).
2. Das, D., Maity, S., Chatterjee, B. & Sen, S. Enabling Covert Body Area Network using Electro-Quasistatic Human Body Communication. *Sci. Rep.-Uk.* **9**, (2019).
3. Bariya, M., Nyein, H. Y. Y. & Javey, A. Wearable sweat sensors. *Nature Electronics.* **1**, 160–171 (2018).
4. Kim, J. et al. Wearable smart sensor systems integrated on soft contact lenses for wireless ocular diagnostics. *Nat. Commun.* **8**, (2017).

5. Ma, Z. et al. High-Reliability and Low-Latency Wireless Communication for Internet of Things: Challenges, Fundamentals, and Enabling Technologies. *IEEE Internet of Things Journal*. **6**, 7946–7970 (2019).
6. Li, N. et al. Large-scale flexible and transparent electronics based on monolayer molybdenum disulfide field-effect transistors. *Nature Electronics*. **3**, 711–717 (2020).
7. Wang, B. et al. Flexible and stretchable metal oxide nanofiber networks for multimodal and monolithically integrated wearable electronics. *Nat. Commun.* **11**, (2020).
8. I, C., Han, S. & Bian, S. Energy-efficient 5G for a greener future. *Nature electronics*. **3**, 182–184 (2020).
9. Shahzad, F. et al. Electromagnetic interference shielding with 2D transition metal carbides (MXenes). *Science*. **353**, 1137–1140 (2016).
10. Cao, W. et al. Binary Strengthening and Toughening of MXene/Cellulose Nanofiber Composite Paper with Nacre-Inspired Structure and Superior Electromagnetic Interference Shielding Properties. *Acs Nano*. **12**, 4583–4593 (2018).
11. Arabi, T. R., Murphy, A. T., Sarkar, T. K., Harrington, R. F. & Djordjevic, A. R. On the modeling of conductor and substrate losses in multiconductor, multielectric transmission line systems. *Ieee T. Microw. Theory*. **39**, 1090–1097 (1991).
12. Ulaby, F. T., Michielssen, E., Ravaioli, U. *Fundamentals of Applied Electromagnetics*. 2016.
13. Asci, C., Sadeqi, A., Wang, W., Rezaei Nejad, H. & Sonkusale, S. Design and implementation of magnetically-tunable quad-band filter utilizing split-ring resonators at microwave frequencies. *Sci. Rep.-Uk*. **10**, (2020).
14. Kaim, V. et al. Ultra-Miniature Circularly Polarized CPW-Fed Implantable Antenna Design and its Validation for Biotelemetry Applications. *Sci. Rep.-Uk*. **10**, (2020).
15. Ferrari, A. C. et al. Science and technology roadmap for graphene, related two-dimensional crystals, and hybrid systems. *Nanoscale*. **7**, 4598–4810 (2015).
16. Guna, V. K. et al. Plant-Based Completely Biodegradable Printed Circuit Boards. *Ieee T. Electron Dev*. **63**, 4893–4898 (2016).
17. Awasthi, A. K., Li, J., Koh, L. & Ogunseitan, O. A. Circular economy and electronic waste. *Nature Electronics*. **2**, 86–89 (2019).
18. Yun, X., Xiong, Z., Tu, L., Bai, L. & Wang, X. Hierarchical porous graphene film: An ideal material for laser-carving fabrication of flexible micro-supercapacitors with high specific capacitance. *Carbon*. **125**, 308–317 (2017).
19. Liu, Y. et al. Rapid roll-to-roll production of graphene films using intensive Joule heating. *Carbon*. **155**, 462–468 (2019).
20. Pan, K. et al. Sustainable production of highly conductive multilayer graphene ink for wireless connectivity and IoT applications. *Nat. Commun.* **9**, (2018).
21. Nayak, P. K. Direct Growth of Graphene on Insulator Using Liquid Precursor Via an Intermediate Nanostructured State Carbon Nanotube. *Nanoscale Res. Lett.* **14**, (2019).

22. Jaakkola, K., Sandberg, H., Lahti, M. & Ermolov, V. Near-Field UHF RFID Transponder With a Screen-Printed Graphene Antenna. *IEEE Transactions on Components, Packaging and Manufacturing Technology*. **9**, 616–623 (2019).
23. Dashti, M. & Carey, J. D. Graphene Microstrip Patch Ultrawide Band Antennas for THz Communications. *Adv. Funct. Mater.* **28**, 1705925 (2018).
24. Wang, Y. et al. Reduced graphene oxide film with record-high conductivity and mobility. *Mater. Today*. **21**, 186–192 (2018).
25. Paton, K. R. et al. Scalable production of large quantities of defect-free few-layer graphene by shear exfoliation in liquids. *Nat. Mater.* **13**, 624–630 (2014).
26. Teng, C. et al. Ultrahigh Conductive Graphene Paper Based on Ball-Milling Exfoliated Graphene. *Adv. Funct. Mater.* **27**, 1700240 (2017).
27. Xin, G. et al. Large-Area Freestanding Graphene Paper for Superior Thermal Management. *Adv. Mater.* **26**, 4521–4526 (2014).
28. Shen, B., Zhai, W. & Zheng, W. Ultrathin Flexible Graphene Film: An Excellent Thermal Conducting Material with Efficient EMI Shielding. *Adv. Funct. Mater.* **24**, 4542–4548 (2014).
29. Song, R. et al. Sandwiched Graphene Clad Laminate: A Binder-Free Flexible Printed Circuit Board for 5G Antenna Application. *Adv. Eng. Mater.* **22**, 2000451 (2020).
30. Fan, C. et al. Electromagnetic shielding and multi-beam radiation with high conductivity multilayer graphene film. *Carbon*. **155**, 506–513 (2019).
31. Iqbal, A. et al. Anomalous absorption of electromagnetic waves by 2D transition metal carbonitride Ti₃CNT_x (MXene). *Science*. **369**, 446 (2020).
32. Sarycheva, A. et al. 2D titanium carbide (MXene) for wireless communication. *Science advances*. **4**, u920 (2018).
33. He, P., Cao, M., Cao, W. & Yuan, J. Developing MXenes from Wireless Communication to Electromagnetic Attenuation. *NANO-MICRO LETTERS*. **13**, (2021).
34. Tran, T. S., Dutta, N. K. & Choudhury, N. R. Graphene inks for printed flexible electronics: Graphene dispersions, ink formulations, printing techniques and applications. *Adv. Colloid Interfac.* **261**, 41–61 (2018).
35. Sa Don, S. N. H. et al. Analysis of Graphene Antenna Properties for 5G Applications. *Sensors-Basel*. **19**, 4835 (2019).
36. Feng, S., Yao, T., Lu, Y., Hao, Z. & Lin, S. Quasi-industrially produced large-area microscale graphene flakes assembled film with extremely high thermoelectric power factor. *Nano Energy*. **58**, 63–68 (2019).
37. Yang, Q. et al. Ultrathin graphene-based membrane with precise molecular sieving and ultrafast solvent permeation. *Nat. Mater.* **16**, 1198–1202 (2017).
38. Xin, G. et al. Highly thermally conductive and mechanically strong graphene fibers. *Science*. **349**, 1083–1087 (2015).

39. Cançado, L. G. et al. General equation for the determination of the crystallite size L_a of nanographite by Raman spectroscopy. *Appl. Phys. Lett.* **88**, 163106 (2006).
40. Xin, G. et al. Microfluidics-enabled orientation and microstructure control of macroscopic graphene fibres. *Nat. Nanotechnol.* **14**, 168–175 (2019).
41. Braunovic et al. Electrical contacts. *CRC Press*, 2007.
42. Leng, T. et al. Graphene Nanoflakes Printed Flexible Meandered-Line Dipole Antenna on Paper Substrate for Low-Cost RFID and Sensing Applications. *Ieee Antenn. Wirel. Pr.* **15**, 1565–1568 (2016).
43. Li, X. et al. Self-reinforcing graphene coatings on 3D printed elastomers for flexible radio frequency antennas and strain sensors. *FLEXIBLE AND PRINTED ELECTRONICS.* **2**, (2017).
44. Akbari, M. et al. Fabrication and Characterization of Graphene Antenna for Low-Cost and Environmentally Friendly RFID Tags. *Ieee Antenn. Wirel. Pr.* **15**, 1569–1572 (2016).
45. Huang, X. et al. Binder-free highly conductive graphene laminate for low cost printed radio frequency applications. *Appl. Phys. Lett.* **106**, 203105 (2015).
46. Wang, W. et al. High-performance printable 2.4 GHz graphene-based antenna using water-transferring technology. *Sci Technol Adv Mater.* **20**, 870–875 (2019).
47. Li, Y., Sim, C., Luo, Y. & Yang, G. 12-Port 5G Massive MIMO Antenna Array in Sub-6GHz Mobile Handset for LTE Bands 42/43/46 Applications. *IEEE Access.* **6**, 344–354 (2018).
48. Song, R. et al. Wideband and low sidelobe graphene antenna array for 5G applications. *Science Bulletin*, (2020).
49. Song, R. et al. A Graphene-Assembled Film Based MIMO Antenna Array with High Isolation for 5G Wireless Communication. *Applied Sciences.* **11**, 2382 (2021).
50. Barreiro, A., Börrnert, F., Rummeli, M. H., Büchner, B. & Vandersypen, L. M. K. Graphene at High Bias: Cracking, Layer by Layer Sublimation, and Fusing. *Nano Lett.* **12**, 1873–1878 (2012).
51. Akbari, A. et al. Highly Ordered and Dense Thermally Conductive Graphitic Films from a Graphene Oxide/Reduced Graphene Oxide Mixture. *Matter.* **2**, 1198–1206 (2020).

Figures

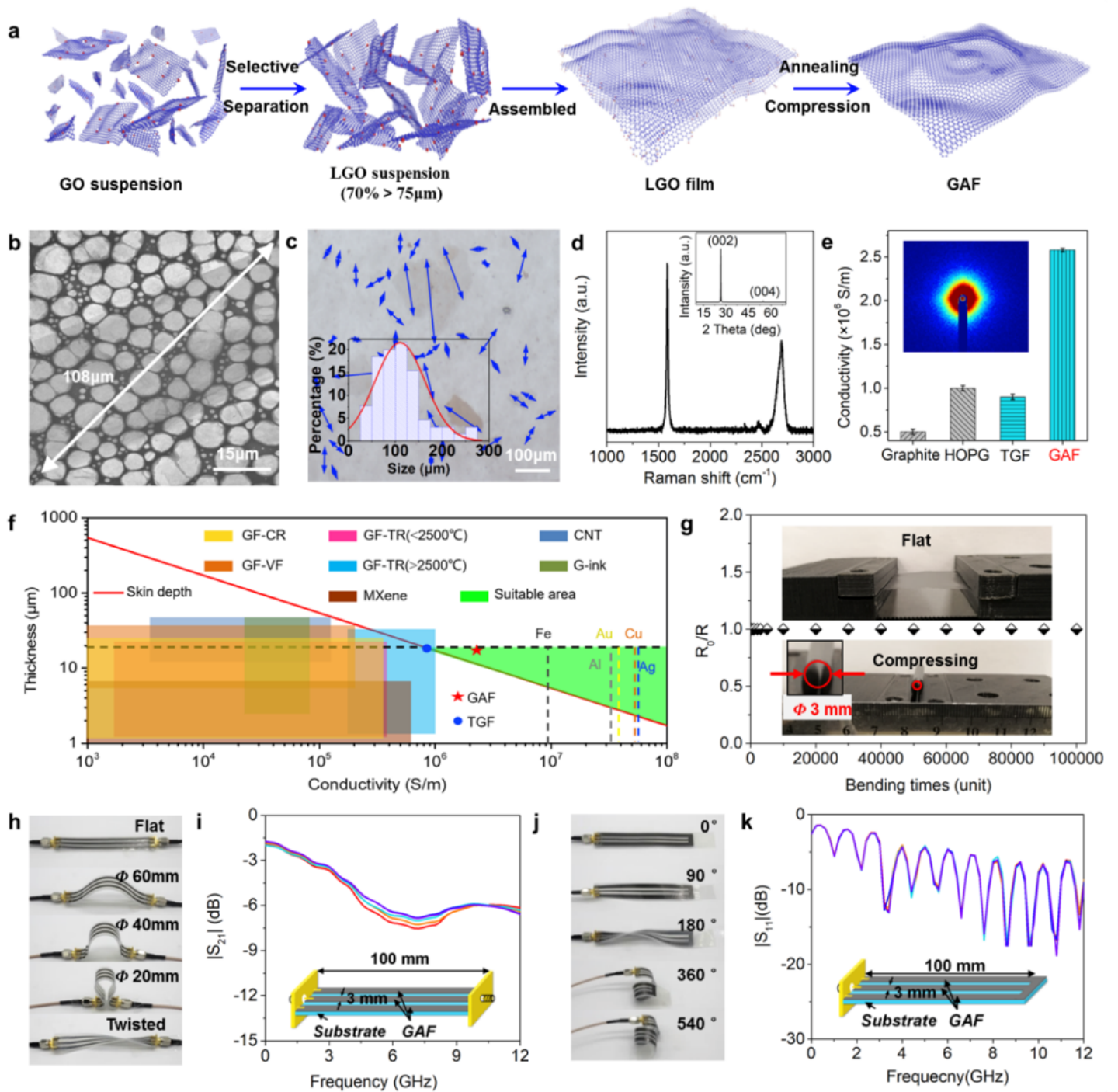


Figure 1

Graphene assembled film fabrication process and characterization. (a) Schematic illustrations of fabrication process of GAF, showing GO selection process, secondary annealing and compression; (b) TEM image of a typical large-sized GO sheet with a lateral size of 108 μm ; (c) Optical microscope image of LGO sheets preparing via drop casting LGO solution on SiO₂ surface; the inserted is a statistic study corresponding LGO size distributions; (d) GAF's XRD pattern and Raman spectrum; (e) A summary of conductivities of GAF, graphite, HOPG and TGF, the insert is SAXS pattern; (f) Skin depth at 860 MHz associate with electrical conductivity and conductive layer thickness of graphene film (GF) prepared by chemical reduction (CR), vacuum filtration (VF), thermal reduction (TR) GO film and other methods,

graphene ink (G-ink), carbon nanotubes (CNT) and MXene; (g) Resistance change of GAF with 100,000 repeating bending test to proof durable flexibility and stability; (h) Flexible GAF FCPW TL being bent with diameters of 60mm, 40mm, 20mm and twisted 180°; (i) Transmission coefficient of the FCPW TL in different states between 10 MHz to 40 GHz frequency band (red-flat, orange-60 mm, wathet-40 mm, blue-20 mm, and purple-twisted); (j) Flexible GAF $\lambda/4$ short-circuited resonator at diffident twisting condition: un-twisted, twisted 90°, 180°, 360° and 540°; (k) Resonator's reflection coefficient results at different twisting condition, between 10 MHz to 12 GHz frequency band (red-flat, orange-90°, wathet-180°, blue-360°, and purple-540°).

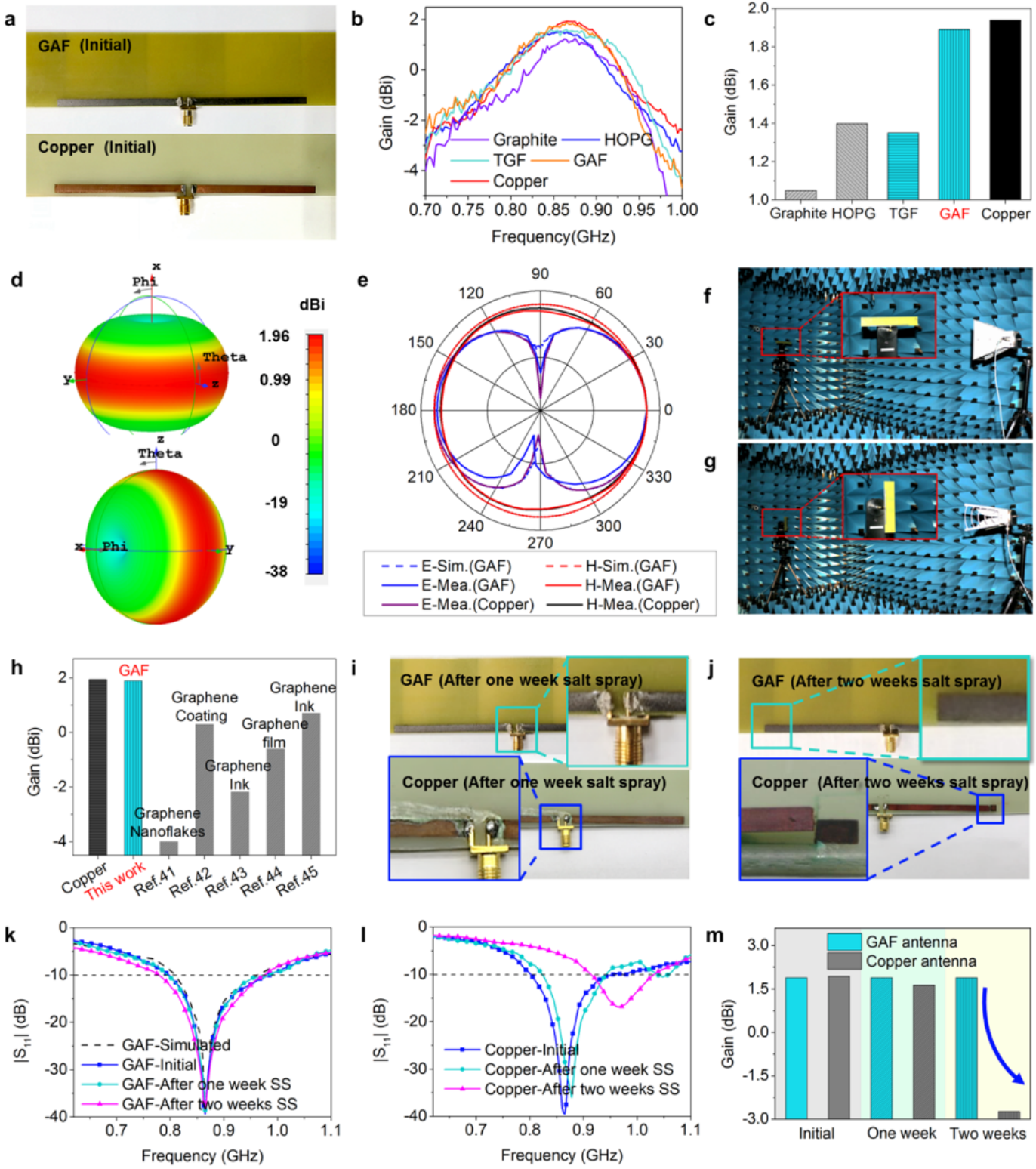


Figure 2

GAF as a dipole antenna and its anti-corrosion performance. (a) Digital photos of GAF and copper dipole antennas, (b) The measured gain of different materials based antennas in BW; (c) The gain of different materials based antennas at 865 MHz; (d) 3D radiation pattern simulation of GAF antenna; (e) Radiation patterns at E-plane and H-plane of GAF and copper antennas; (f, g) Measurement environments of radiation pattern at E-plane and H-plane, respectively; (h) Comparison of the dipole antenna gain in

references with the results in this work; (i, j) Digital photo of GAF and copper dipole antennas after one week and two weeks salt spray; (k) Measured and simulated $|S_{11}|$ of GAF antenna, initial, after one week and two weeks salt spray; (l) Measured $|S_{11}|$ of copper antenna, initial, after one week and two weeks salt spray; (m) The measured gain of GAF and copper antennas at 865 MHz with initial, after one week and two weeks salt spray.

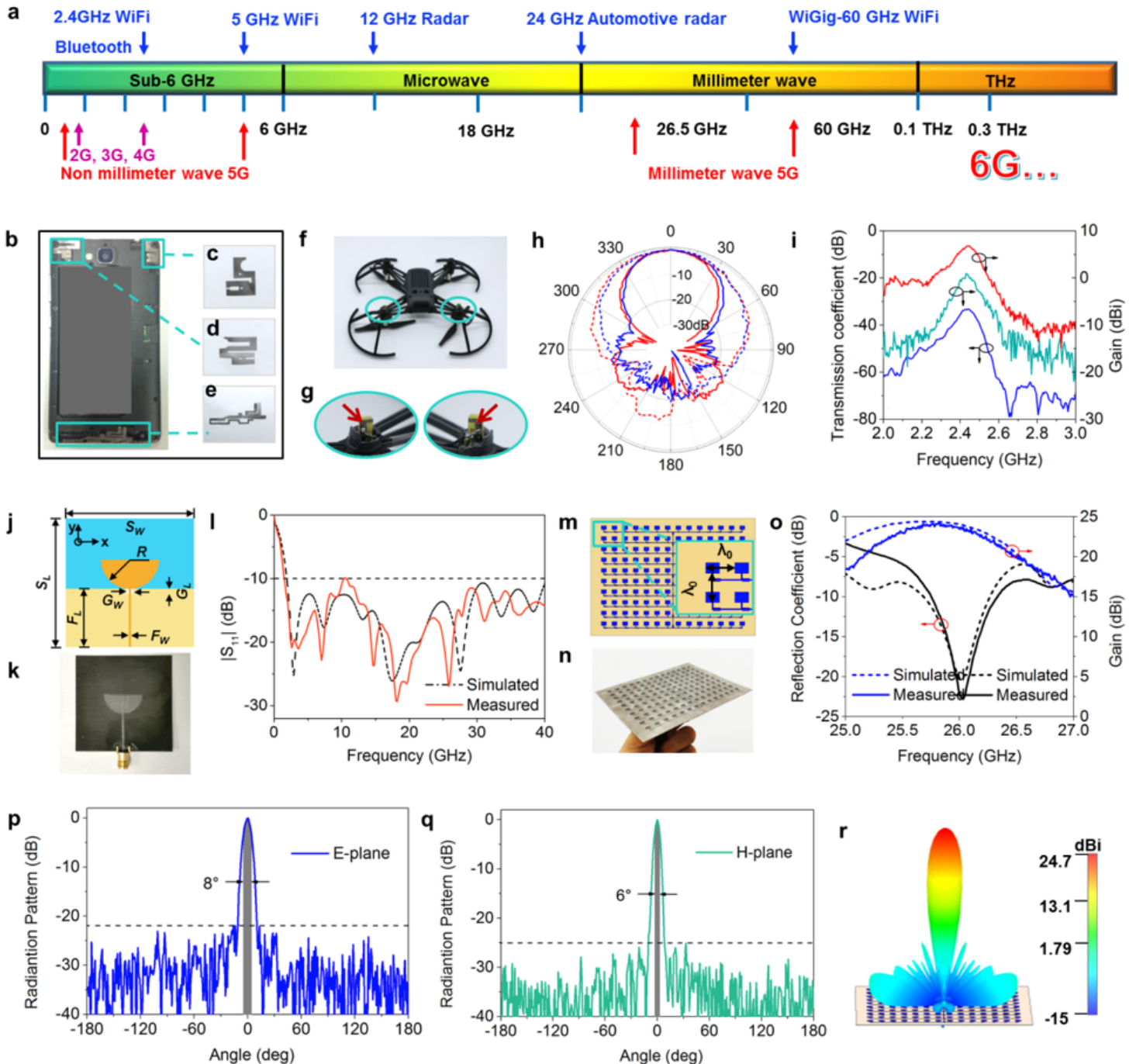


Figure 3

GAF applied in Sub-6GHz wireless communication system and millimeter wave antenna. (a) The division of wireless communication spectrum with specified applications; (b) Digital photo of mobile phone with GAF antennas; Digital photo of zoomed GAF mobile phone antennas: (c) Bluetooth antenna, (d) WiFi

antenna and (e) main communication antenna; (f) Digital photos of drone with GAF antennas; (g) Digital photo of zoomed GAF drone antennas; (h) The measured radiation patterns of GAF wearable antenna and antenna array, the dashed and solid lines are the radiation patterns of the wearable antenna and the antenna array respectively, the red line is E-plane, and the blue line is H-plane; (i) Measured transmission coefficient (blue line), gain of GAF antenna array (red line) and wearable antenna (green line); (j) Structure of the GAF UWB antenna, overall size of UWB, $SL=SW=50$ mm; $R=10$ mm, $FL=20$ mm, $FW=0.8$ mm, $GL=0.7$ mm, $GW=1$ mm; (k) Digital photo of the GAF UWB antenna; (l) Measured and simulated $|S_{11}|$ of the UWB antenna; (m) Schematic diagram of the GAF millimeter wave antenna array with the element spacing of $3/4\lambda$; (n) Digital photo of GAF millimeter 5G antenna array with 140 elements; (o) Measured and simulated reflection coefficient and gain of GAF 5G millimeter wave antenna array; (p, q) Measured E-plane and H-plane radiation patterns and (r) the simulated three-dimensional radiation patterns of GAF 5G millimeter wave antenna array.

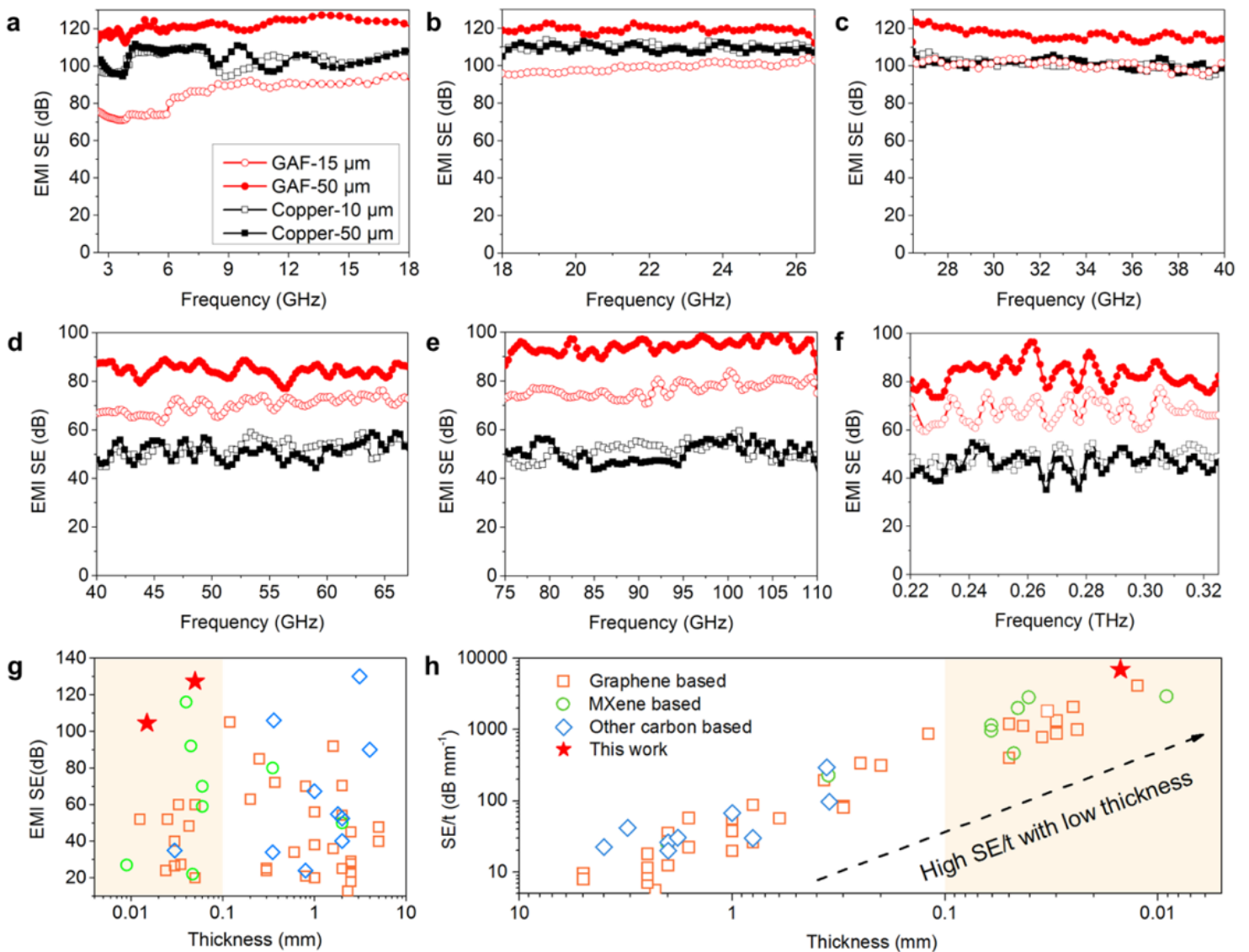


Figure 4

GAF applied in EMI protection. (a-f) In the frequency range of 2.6 GHz - 0.32 THz, EMI SE of GAF with 15 μm and 50 μm thickness and copper with 10 μm and 50 μm thickness, (a) 2.6-18 GHz (rectangular waveguide method), (b) 18-26.5 GHz (rectangular waveguide method), (c) 26.5-40 GHz (rectangular waveguide method), (d) 40-67 GHz (free space method), (e) 75-110 GHz (free space method) and (f) 0.22-0.3235 THz (free space method); (g, h) a comparison of SE and SE/t in references with the results in this work (the best results for the frequency bands given in the literature).

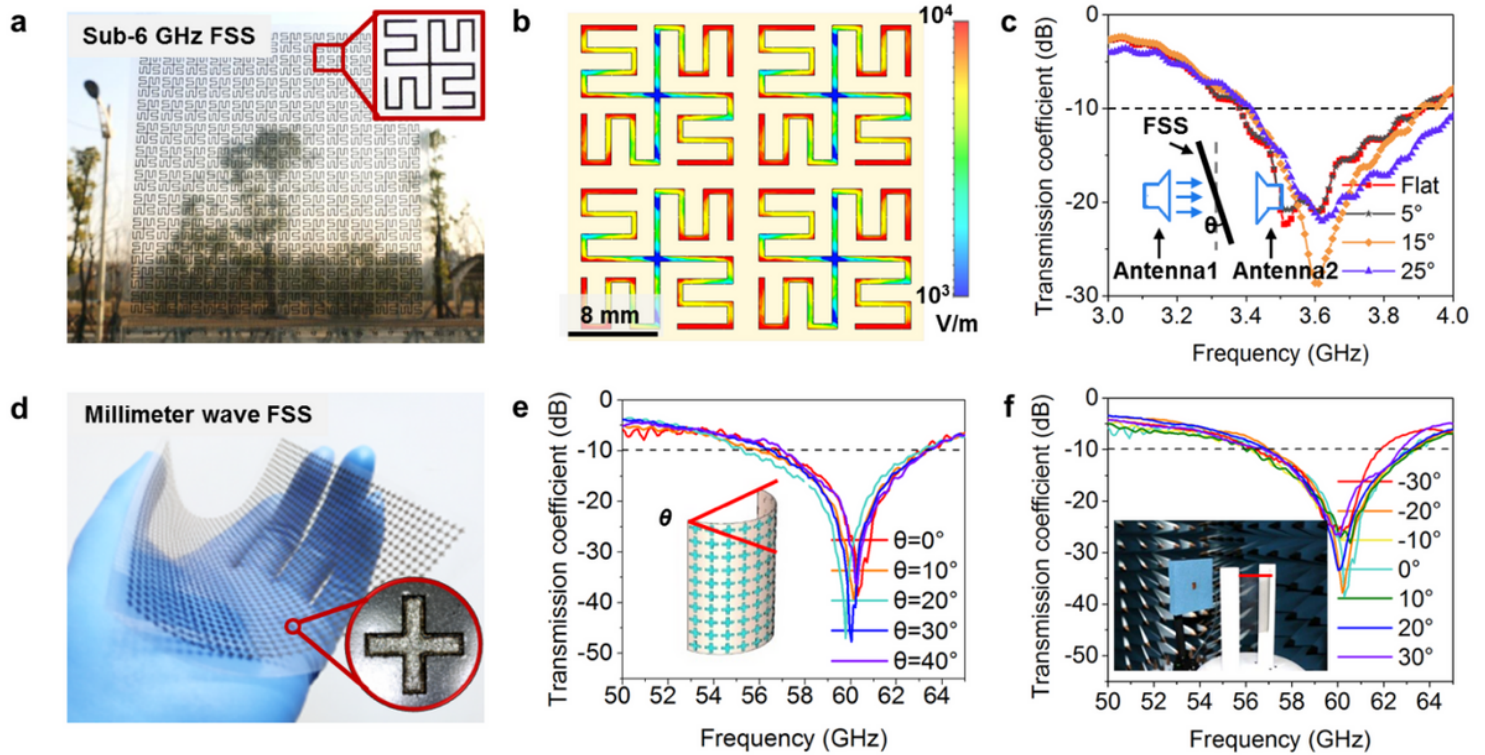


Figure 5

GAF based FSS. (a) The digital photo of Sub-6 GHz translucent GAF FSS, with 12×12 elements; (b) E-field distribution of GAF FSS at 3.5 GHz; (c) The transmission coefficient of GAF FSS in incident obliquely of electromagnetic wave; (d) The digital photos of millimeter wave translucent GAF FSS with 40×40 elements; (e, f) The transmission coefficient of GAF FSS in different bending state and incident obliquely of electromagnetic wave.

Supplementary Files

This is a list of supplementary files associated with this preprint. Click to download.

- [SupplementaryInformation.docx](#)
- [VideoS1Conductivitytest.mp4](#)
- [VideoS2Mechanicalstabilitytest.mp4](#)
- [VideoS3Grapheneantennadrone.mp4](#)
- [VideoS4Grapheneantennaphone.mp4](#)